ARL-TR-10032 ● Dec 2024

Packing Behavior and Permeability of Mono- and Bimodal Mixtures of Coarse Granular Diamond Grit as Precursors for Reaction Bonding of Diamond–Silicon Carbide (SiC) Composites

by Anthony DiGiovanni and Clifford Hubbard

NOTICES

Disclaimers

The findings in this report are not to be construed as an official Department of the Army position unless so designated by other authorized documents.

Citation of manufacturer's or trade names does not constitute an official endorsement or approval of the use thereof.

Destroy this report when it is no longer needed. Do not return it to the originator.

ARL-TR-10032 ● DEC 2024

Packing Behavior and Permeability of Mono- and Bimodal Mixtures of Coarse Granular Diamond Grit as Precursors for Reaction Bonding of Diamond–Silicon Carbide (SiC) Composites

Anthony DiGiovanni and Clifford Hubbard
DEVCOM Army Research Laboratory

REPORT DOCUMENTATION PAGE

1. REPORT DATE	2. REPORT TYPE	3. DATES COVERED	
		START DATE	END DATE
December 2024	Technical Report	10/01/2023	9/29/2024

4. TITLE AND SUBTITLE
Packing Behavior and Permeability of Mono- and Bimodal Mixtures of Coarse Granular Diamond Grit as Precursors for Reaction Bonding of Diamond–Silicon Carbide (SiC) Composites

5a. CONTRACT NUMBER	5b. GRANT NUMBER	5c. PROGRAM ELEMENT NUMBER
5d. PROJECT NUMBER	5e. TASK NUMBER	5f. WORK UNIT NUMBER

6. AUTHOR(S)
Anthony DiGiovanni and Clifford Hubbard

7. PERFORMING ORGANIZATION NAME(S) AND ADDRESS(ES)
DEVCOM Army Research Laboratory
ATTN: FCDD-RLA-ME
Aberdeen Proving Ground, MD 21005

8. PERFORMING ORGANIZATION REPORT NUMBER
ARL-TR-10032

9. SPONSORING/MONITORING AGENCY NAME(S) AND ADDRESS(ES)	10. SPONSOR/MONITOR'S ACRONYM(S)	11. SPONSOR/MONITOR'S REPORT NUMBER(S)

12. DISTRIBUTION/AVAILABILITY STATEMENT
DISTRIBUTION STATEMENT A. Approved for public release: distribution unlimited.

13. SUPPLEMENTARY NOTES
ORCID: Anthony DiGiovanni, 0000-0003-3344-1753

14. ABSTRACT
Packing and permeability relationships in bimodal mixtures of 125- and 25-µm diamond powders were evaluated and compared with established theoretical and empirical relationships for similar-sized spherical powders for future correlations with liquid silicon infiltration (LSI) reaction bonded composite synthesis of diamond composites. Diamond powders were characterized via scanning electron microscopy and laser particle size analysis. The packing characteristics were determined using a commercial tap densometer with 125-µm diamond packing to 64.4% and 25-µm packing to 60.6%. Falling head permeability testing was used to determine corresponding values of 9.34×10^{-12} m^2 for the 125-µm diamond packing and 5.31×10^{-13} m^2 for the 25-µm diamond packing. Reasonable agreement was found in the packing characteristics with empirical calculations and theoretical computation. Peak permeability was estimated at 40 vol%, 125-µm diamond in the bimodal mixtures, which suggests that optimizing LSI composite formulas near this condition may improve density and reduce residual silicon.

15. SUBJECT TERMS
Sciences of Extreme Materials, particle packing, permeability, diamond, silicon carbide, melt infiltration

16. SECURITY CLASSIFICATION OF:			17. LIMITATION OF ABSTRACT	18. NUMBER OF PAGES
a. REPORT	b. ABSTRACT	C. THIS PAGE		
UNCLASSIFIED	UNCLASSIFIED	UNCLASSIFIED	UU	30

19a. NAME OF RESPONSIBLE PERSON	19b. PHONE NUMBER *(Include area code)*
Anthony DiGiovanni	(410) 306-4587

STANDARD FORM 298 (REV. 5/2020)
Prescribed by ANSI Std. Z39.18

Contents

List of Figures

List of Tables

1. Introduction

Powdered or particulate systems are common in many disciplines and industries, such as chemistry, physics, civil and geotechnical engineering, pharmaceuticals, food industries, and materials science.[1] All share concerns about the size, distribution, and shape of particles in their respective systems and how that affects processes and measurements on which they depend.[2] In materials science, powder-based processing is foundational to a broad range of synthesis techniques and requires substantial knowledge and control of packing and flowability of powder assemblies to achieve optimized material performance. While the synthesis of many materials, especially metals and ceramics, is based on processing powders that consolidate under the application of increasing temperature through mass transport via sintering,[3,4] some composite materials form at lower temperatures that do not rely predominately on sintering. One example under consideration as part of this investigation is reactive metal infiltration (RMI).[5] Commonly used to create lower-cost, near-net-shaped materials (especially composites), RMI is an established commercialized technique to synthesize a wide range of composite materials, especially carbon-based composites using fibers or powders, for many engineering applications.[6–10] When the reactive metal is silicon, this process is often referred to as liquid silicon infiltration (LSI).[11] Despite the differing densification methods—RMI versus thermally diffusive mass transport—both approaches depend strongly on the underlying composite structure (often powders or fibers) to achieve optimal densification.

While recent research suggests that the RMI of powder-based composites can deviate from fundamental Washburn capillarity, stemming from interfacial chemical reactions affecting wetting angle of the infiltrant,[12,13] the underlying pore structure determined by the compacted particles nevertheless contributes meaningfully to flow, especially as porosity is reduced. Moreover, other important factors that influence the infiltration, reaction, and densification of LSI composite structures include the amount, type, and distribution of available carbon for silicon to interact with.[9–11,14] Additionally, the viscosity of molten silicon at its melting point (1414 °C) is approximately 1 centipoise,[15,16] roughly equivalent to water at room temperature. Therefore, it is hypothesized that by optimizing the underlying particle structure, and thereby the attendant pore structure, first-order benefits to the RMI process can be evaluated and improved using standard water-based permeability measurements. The optimized powder size distributions will guide similarly optimized final infiltrated composite density and improved LSI composite material synthesis. This investigation establishes a preliminary understanding of

how bimodal granular diamond compacts pack together and subsequently influence fluid flow through packed structures.

2. Particle Packing

Understanding the influence of the powder morphology and packing characteristics on RMI necessitates understanding the behavior of how the constituent powders or granular materials mix, flow, and consolidate under the influence of gravity or applied forces prior to implementing temperature-activated processes. Many empirically derived metrics, often aligned with specific disciplines or industrial needs, have been devised to track and measure powder characteristics and are too varied to cover in detail here. The powder characteristics evaluated in this study are bulk density or apparent density (the amount of powder mass within the observed volume that contains the powder) and are represented as a fractional packing percentage, f_p. The poured bulk density or loose density is the fractional packing of the powder when it is removed from a container or mixing process and transferred to another vessel; it is often the lowest value or loosest packing arrangement of the powder. When the residual porosity is zero, the powder is fully consolidated, and the apparent density is equivalent to the intrinsic material density of the powder grain. The poured density is not a constant and depends on many different conditions prior to making the measurement. By comparison, the tap density, though still sensitive to external conditions such as humidity, is significantly more deterministic and is defined as the asymptotic change in bulk density of the powder after vertical tapping of a prescribed amplitude, frequency, and duration.[17]

Characterization standards have been established for packing powders or granular materials,[18,19] with tap density being a preferred metric. When combined with bulk density, tap density can help determine the flowability of the powder, which is useful for handling and die-filling considerations. The poured density is always less than the tap density, though the two measurements will approach equality as the mean particle size increases and the weight of the particle overcomes smaller interparticle forces associated with humidity and/or Van der Waals forces that promote aggregation and clumping.[20]

The ability of particles to pack densely and uniformly depends on many factors, including the individual particle shapes, the mean particle sizes, the number and volume fraction of particle distributions, and their statistical characteristics.[21,22] Particle packing theory is well established and derives from early work by Furnas, Andreasen, and Westman.[23–26] Furnas' research established the packing behavior of discrete binary mixtures of particles, whereas Andreasen's work was similar but focused on continuous particle size distributions. A key result from Furnas' work

is shown in Figure 1 where the specific volume of a binary mixture of two different size particles, one larger than the other, is shown. The leftmost part of the graph is purely small particles, and the rightmost part of the graph is purely large particles, with intermediate regions a mixture of the two. The 100% dense marker line indicates the theoretical material density, ρ_t, (or volume) where porosity has been eliminated. The high points on the y-axis extremities indicate a specific volume for random close packing (RCP) of spheres ($1.57\rho_t$[27]) and are equivalent. As the two sizes are mixed, smaller particles begin to fit inside the open spaces between the larger particles. When the ratio of diameters of large and small particles is sufficiently large, an optimal packing condition—maximum apparent density—is attained.[21] For frictionless spherical particles, the functional dependence of optimal packing shifts the peak towards lower concentrations of large particles. However, for size ratios of 7:1 or greater, optimal packing will be achieved with approximately two-thirds of the particles being the larger size.

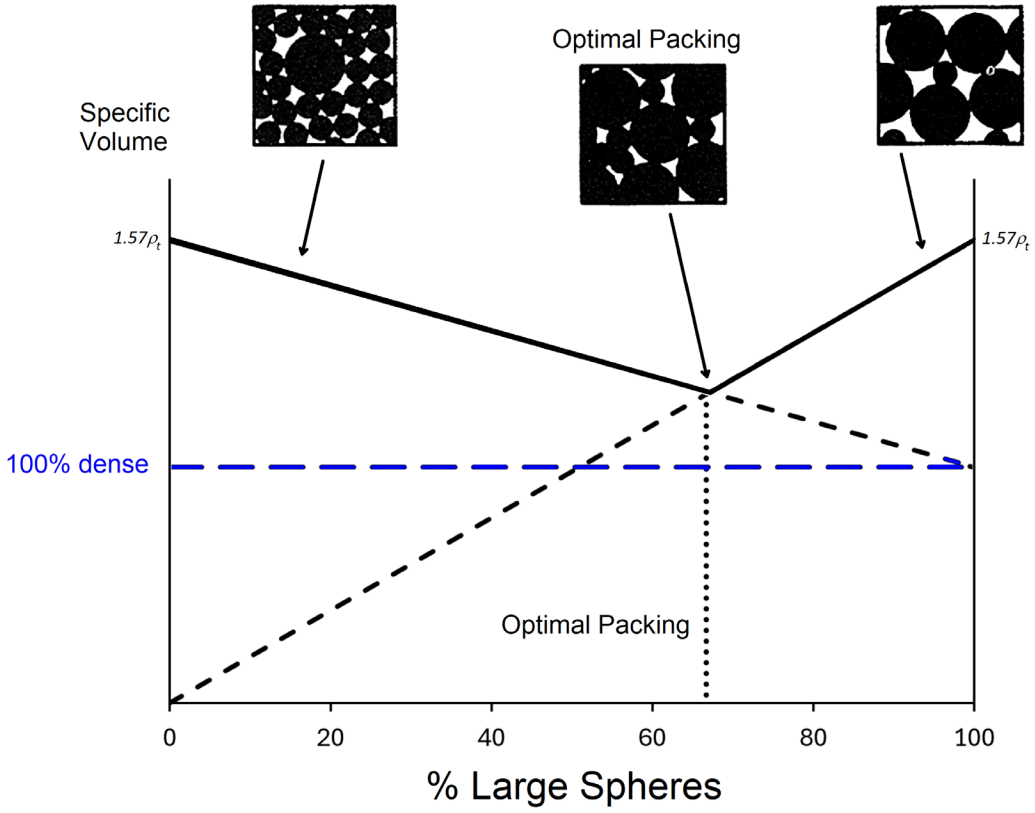

Figure 1. Bimodal packing relationship for idealized sphere mixtures of arbitrary small and large spheres. Optimal packing of spheres and corresponding density are achieved at an intermediate volume mixture of large and small spheres. The full material density, in the absence of any porosity, is shown by the horizontal dashed line. After German.[21]

The experimental, theoretical, and computational studies that have taken place since that early work are too numerous to list here, but notable work by McGeary on discrete particle mixtures with steel ball bearings illustrated the practical benefits of bimodal packing optimization.[28] Another important contribution, shortly after McGeary's work, is that of Yerazunis et al., which established closed-form relations for arbitrary mixtures of different volume fractions of bimodal particles up to about 80 vol% large, for particle diameter ratios of two or greater.[29] The packing fraction, f_p, can be expressed in terms of the ideal RCP fraction, f_{rcp}, the diameters of large, D_l, and small, D_s, particles, and the volume fraction of large particles, V_l, in the mixture as shown in Equation 1:

$$f_p = \frac{f_{rcp}}{1 - \left[1 - f_{rcp} - \frac{6}{\pi} A \left(\frac{D_s}{D_l}\right)^{1+m}\right] V_l - \frac{6}{\pi} \frac{\left(\frac{D_s}{D_l}\right)^4 {V_l}^2}{(1 - V_l)}} \quad (1)$$

where the constants $A = 0.165$, $B = 0.5$, and $m = -0.294$ were correlated empirically from large datasets. Plots of Equation 1 for D_l/D_s ratios from 2.58 to infinity are shown in Figure 2 with corresponding experimental values. The relationship described in Equation 1 will be applied to the diamond powders and combined with basic permeability relationships as detailed in the Discussion section.

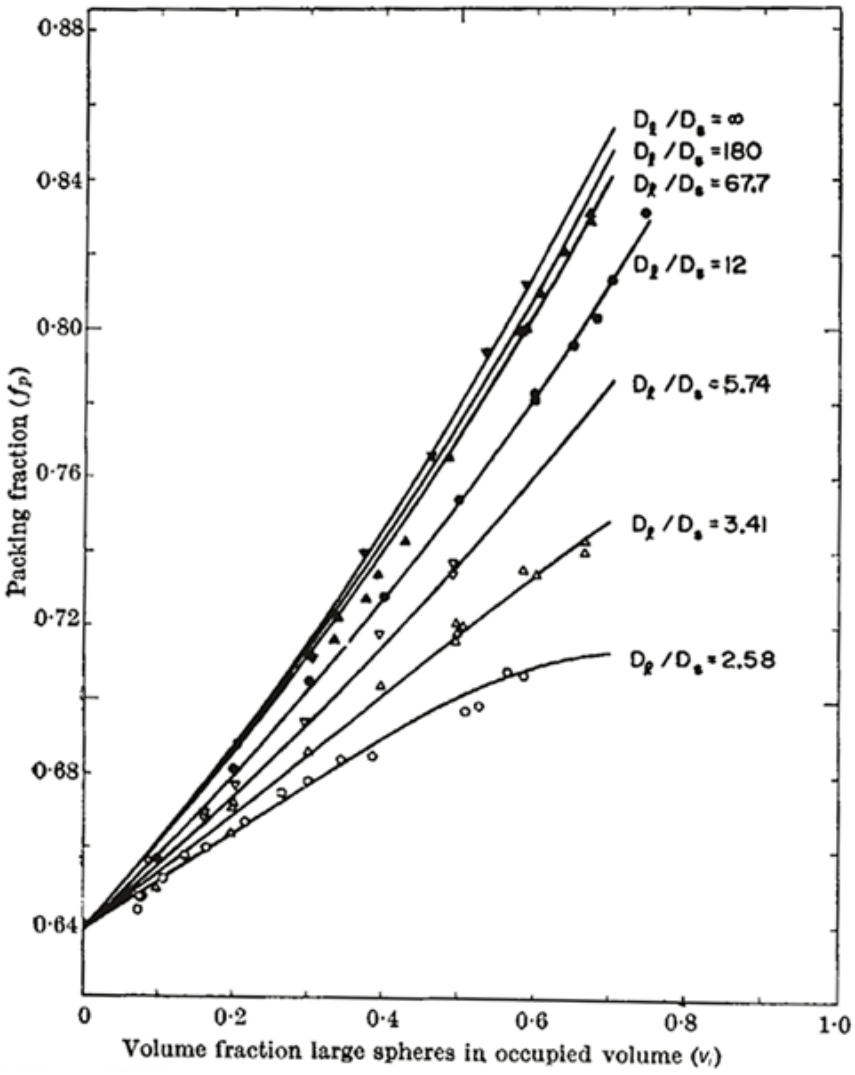

Figure 2. Plots of the packing fraction relationship, f_p vs. V_l, of Equation 1 for monosized bimodal sphere mixtures with size ratios D_l/D_s from 2.58 to infinity (solid lines). Corresponding experimental data is shown as symbols. After Yerazunis et al.[29]

3. Permeability of Granular Materials

Liquid permeability of ideal (low Reynolds number) non-turbulent flow, often referred to as Darcy permeability,[30] through a compacted powder or granules over wide-ranging sizes and distributions has been well characterized as a function of packing fraction. While precise calculations of permeability for compacted powders or other complex structures are not tractable analytically because of the complex nature of equations that govern fluid dynamics, reasonable estimates can be made from empirical relations.[31] One of the simplest and most well-known empirical relationships for granular porous structures is that by Kozeny–Carman,[32] given in Equation 2 as

$$\kappa = \Phi_s^2 \frac{\varepsilon^3 D_p}{180(1-\varepsilon)^2} \quad (1)$$

where κ, is single phase permeability, Φ_s is particle sphericity, ε is porosity of the powder pack, and D_p is the mean particle diameter. The Kozeny–Carman relationship has been found to be reasonably predictive for granular materials above the percolation threshold for open porosity.[31]

Darcy permeability can be measured in the laboratory for many granular materials using an ASTM standardized test apparatus.[33,34] The apparatus, commonly known as a falling (or constant) head permeameter, is used to test a wide range of granular or particulate materials. The test apparatus can be implemented in one of two configurations depending on the permeability of the material being evaluated. Generally, materials with lower hydraulic conductivity ($K < \sim 10^{-4}$ cm/s) employ the falling head test configuration, and the constant head permeability test configuration is used for higher flow rate materials ($K > \sim 10^{-4}$ cm/s). The fine-grain diamond powders in this study were expected to be low hydraulic conductivity based on estimates from Equation 2 and were evaluated using a modified falling head test configuration to account for the small volume of diamond powder available relative to the larger prescribed ASTM standard chamber size. The ASTM standard was developed, in part, for naturally occurring materials such as soil and rock with wide spatial variations in flow properties. By comparison, synthetic diamond powders are expected to be highly uniform and minimize uncertainty associated with smaller sample volume, therefore the smaller test volume is expected to yield valid conductivity results.

Notably, the falling head permeability test does not measure Darcy permeability,[*] k, directly but establishes the hydraulic conductivity of a packed material bed. The hydraulic conductivity, K, is related to the volumetric flow rate, Q, of liquid, the cross-sectional area of the porous material, A, the length of the porous sample traversed by the flow stream, L, and the change in height of the water column (or head), Δh, above the sample as shown in Equation 3:

$$K = \frac{Q \cdot L}{A \cdot \Delta h} \quad (3)$$

Once the hydraulic conductivity has been determined, the Darcy permeability is calculated by multiplying by kinematic viscosity, μ, of the liquid (typically water at ambient conditions), liquid density, ρ, and the gravitational constant, g, as illustrated in Equation 4:

[*] Darcy permeability is conventionally expressed in units of millidarcy (mD). One darcy is equivalent to the flow of 1 cm^3/s of a fluid with the viscosity of 1 centipoise (cP) or 1 mPa·s.

$$k = \frac{K \cdot \mu}{\rho \cdot g} \tag{4}$$

4. Experimental Procedure

4.1 Raw Material Characterization

The formation of reaction-bonded diamond silicon carbide (SiC) composites depends on the starting diamond grit. For this investigation, two grades of granular diamond were used with nominal average grain sizes of 25 and 125 μm (Diamond Scientific Inc.). The 25-μm material is a crushed product, which implies that the grains derived from larger sized particles, were mechanically fragmented, and then sieved to meet the specific size modality. The 125-μm material was purchased as an as-grown cuboctahedral crystal, which was also sieved to meet the specific size requirements but did not receive any mechanical size reduction. Low-magnification scanning electron microscopic (SEM) images using a backscattered electron imaging mode are shown in Figure 3 (Phenom XL, Thermo Fisher Scientific), where the 25-μm image (nominal magnification of 500×) is on the left and the 125-μm image (nominal magnification of 250×) is on the right. Uncoated samples were prepared by pressing conductive carbon tape onto an aluminum stud and then pressing the diamond powders onto the exposed surface of carbon tape. Poorly adhered powder grains were removed with compressed air. Higher-magnification SEM images (Apreo 2 SEM, Thermo Fisher Scientific) of the granular diamond were collected at nominal magnifications of 1000× (Figure 4, right) for the 125-μm diamond and 5000× (Figure 4, left) for the 25-μm diamond grit. The specimens evaluated under high magnification were different from the low-magnification samples and were prepared by coating an aluminum stub with carbon paint and distributing small amounts of powder on the paint before it dried. The stubs were dried overnight in vacuum prior to imaging.

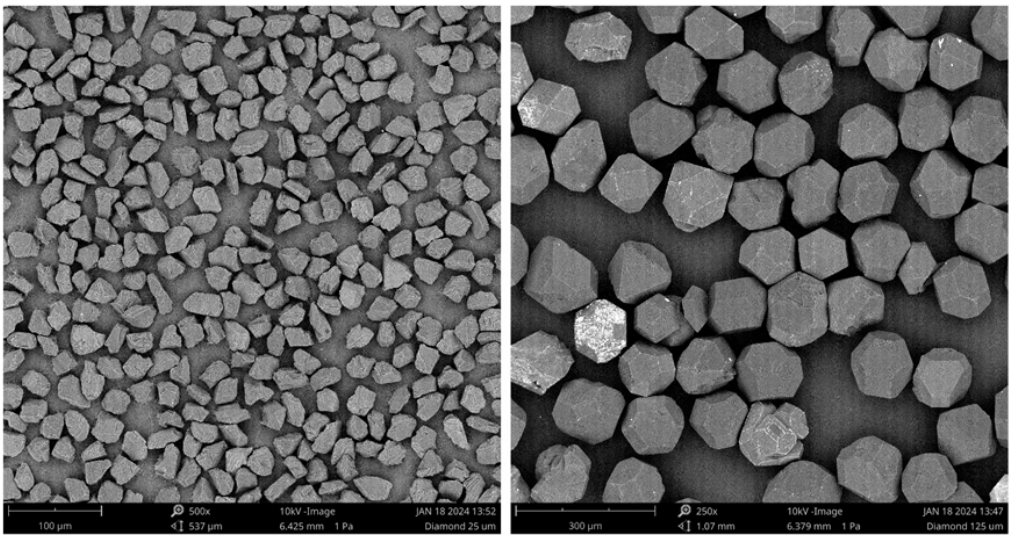

Figure 3. Back-scattered SEM images of the 125-µm diamond at 250× (right) and 25-µm diamond at 500× (left) powders. The 125-µm diamond powder exhibits cuboctahedral faceting from the as-grown crystal, whereas the 25-µm diamond is a crushed and sieved material.

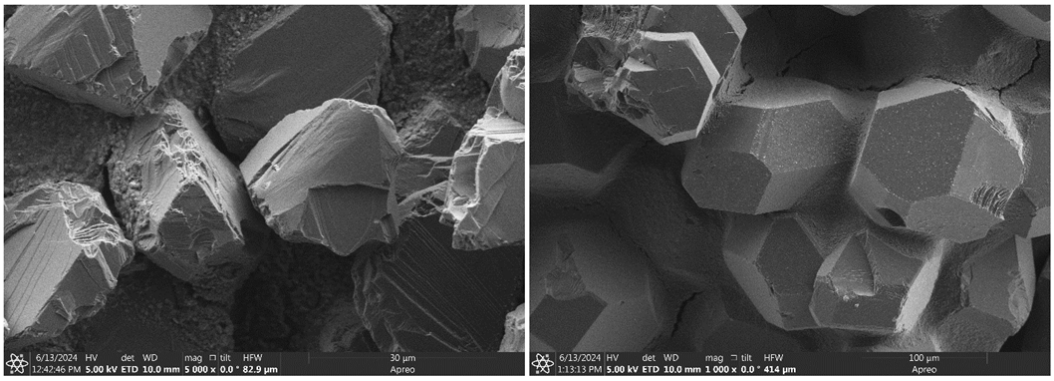

Figure 4. High-resolution back-scattered SEM images of the 125-µm diamond at 1000× (right) and 25-µm diamond at 5000× (left) powders.

Diamond powder size distributions were characterized by laser scattering (Horiba LA-960*) after ultrasonicating in water. Log-frequency plots along with cumulative distribution percentages for each size powder are shown in Figure 5. The statistical summary of the data collected from the laser particle diffraction measurements is shown in Table 1. Although there is no strict standard, generally, a geometric variance less than approximately 1.5 will indicate a narrow distribution for a monomodal powder. Thus, both the diamond powders in this investigation can be considered to have narrow particle size distributions as shown in Table 1.

* Model LA-960 has been discontinued. See www.horiba.com for the latest model or legacy product information.

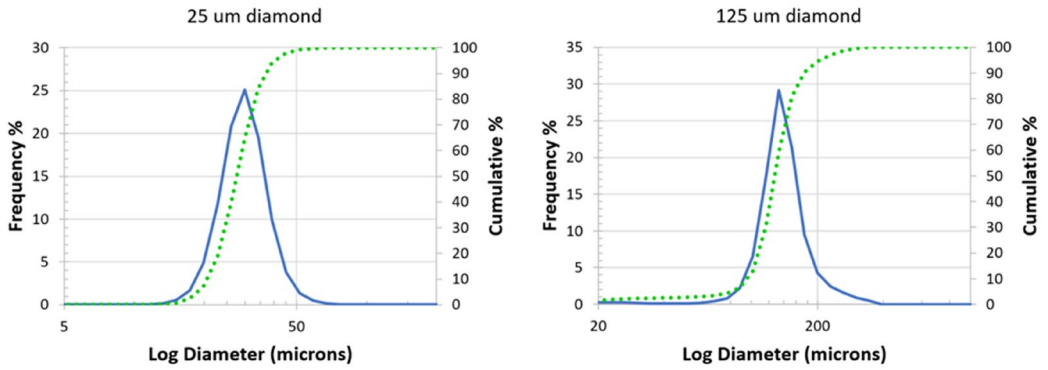

Figure 5. Laser scattering particle size distributions for 125-µm and 25-µm diamond powders. Measured particle sizes are consistent with manufacturer's reported size.

Table 1. Summary of statistical measurements from laser scattering on diamond grit.

Measurement	125 µm	25 µm
Median size (µm)	127.4	27.6
Mean size (µm)	131.8	28.3
St. dev. (µm)	40.7	6.7
Mode size (µm)	125.6	27.8
Geo. mean size (µm)	124.0	27.6
Geo. variance (μm^2)	1.1	1.0
D(v0.1) (µm)	95.2	20.6
D(v0.5) (µm)	127.4	27.6
D(v0.9) (µm)	174.1	37.0

4.2 Powder Mixing

The diamond powder samples in this study ranged from 100% 25-µm diamond to 100% 125-µm diamond with blended mixtures of the two at 20 vol% increments as shown in Table 2. The constituent powders were weighed, with the combined weights shown in Table 2, and placed in a 250-mL Nalgene container for blending.

Table 2. Tap density measurements for diamond powder blends. Sample weight is the amount of powder in the graduated cylinder, the number of taps, and the packing fraction.

125 µm	25 µm	Mean Size µm	wt (g)	# of Taps	Packing fraction
100%	0%	125	10.3	6000	64.4%
80%	20%	105	14.4	9000	82.0%
60%	40%	85	11.9	6000	77.2%
40%	60%	65	11.0	6000	67.6%
20%	80%	45	9.9	3000	63.8%
0%	100%	25	9.1	6000	60.6%

Powder blending was achieved using a 3D shaker mixer shown in Figure 6 (Turbula T2F, WAB-GROUP) for 60 min at 34 revolutions per minute (rpm) to minimize particle segregation.[35]

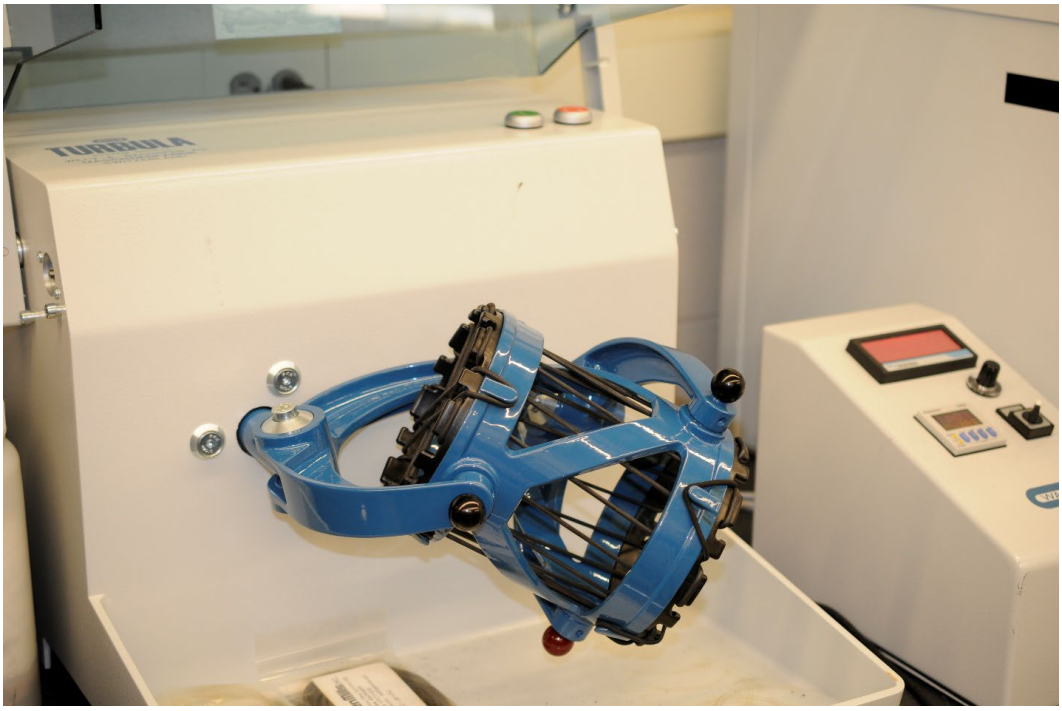

Figure 6. Turbula shaker mixer with adjustable rpm and timer module used for blending diamond powders. Mixing conditions were 60 min at 34 revolutions per minute (rpm).

4.3 Powder Consolidation

Diamond powders listed in Table 2 were consolidated using a commercial tap densometer (Figure 7; Quantachrome Auto TAP AT-6, Anton Paar) with a 10-mL glass graduated cylinder at ambient lab conditions of 20.5 °C and 48% relative humidity. The initial volume of powder was recorded as the apparent bulk density, and then volume measurements were recorded at tap increments of 500, 1500, and 3000. When necessary, additional increments of the 3000-tap cycle were repeated until the measured powder volume was unchanged. The total number of taps for each powder mixture is shown in the fifth column of Table 2.

Figure 7. Tap densometer with 10-mL glass graduated cylinder. Measurements were typically initiated on powder volumes of about 8 mL.

4.4 Permeability Measurements

The basic falling head permeameter (HM-891, Gilson Company, Inc.) is shown in Figure 8 (left) and consists of a graduated central column to hold the head, a ball valve located at the base of the column to control flow, and a funnel, tube, and standardized chamber for the soil or granular material being tested. The chamber is 2.5 inches in diameter and 5 inches tall, which would require exceptionally large volumes of diamond powder to test. To conserve diamond powder, a modified design was implemented in a 5.454-mm-inner-diameter (ID) plastic tube (Figure 8, center). Before filling the plastic tube with diamond powder, the base of the tube was sealed with parafilm. A metal punch with nominally the same ID as the plastic tube was used to cut discs of coarse filter paper, two of which were placed at the bottom of the tube as shown as the blue line in Figure 8 (right). After filling with diamond powder, the tube was placed into the tap densometer using a custom jig. The powder in the small tube was tapped using the same conditions for the larger samples reported earlier. After tapping, the parafilm seal at the bottom of the tube was perforated and the tube was slowly filled with deionized water until fully saturated. To ensure the custom jig was not impeding flow, the flow rate was measured in the same configuration without powder and found to be greater than four times the flow rate of the packed tube.

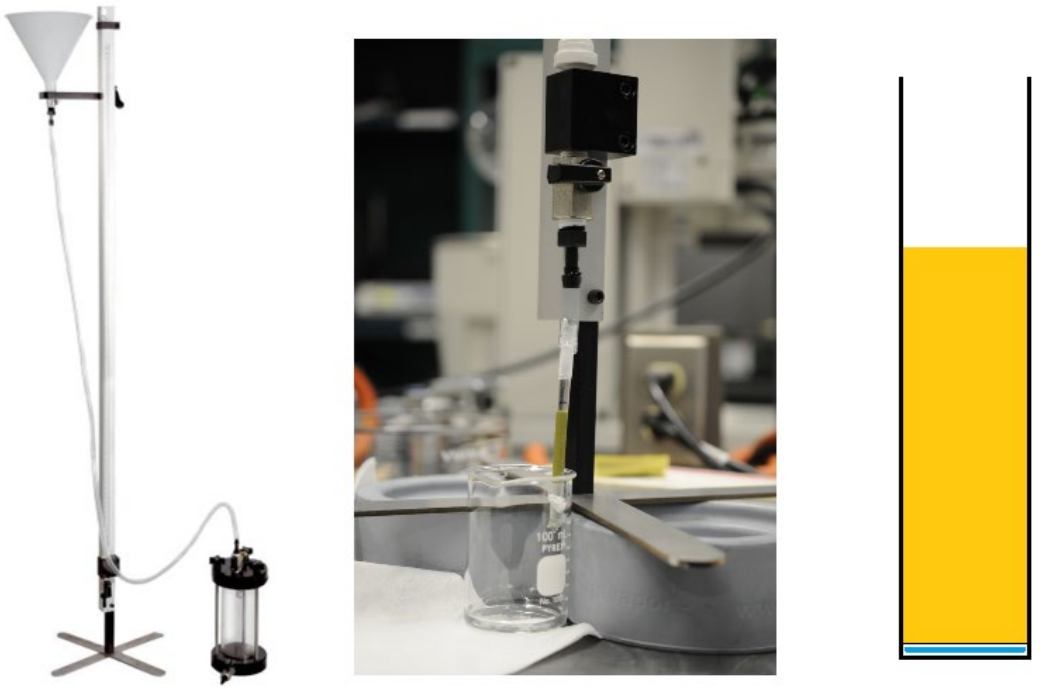

Figure 8. Gilson Company, Inc., HM-891 falling head permeameter setup (left). The traditional particle chamber was removed and replaced with a custom small plastic tube (center) with diamond particles packed to the tap density as shown (right). The plastic tube, open at both ends, was sealed with parafilm on one end, filled with two precut circles of coarse filter paper, then filled with diamond powder and tapped. After tapping, the parafilm was perforated in several locations to allow fluid egress. Fluid flow through the tube without powder was more than four times greater than the packed tube.

The next step is critical to ensuring a valid hydraulic conductivity measurement. The plastic tube was filled to its brim with water and quickly coupled to the bottom of the manometer column just below the valve exit port as shown in Figure 8 (center). The coupled tubes were carefully inspected for air bubbles. Entrained bubbles must be removed, or the connection removed and repeated until there is a continuous, bubble-free, fluid connection between the plastic and manometer tubes. When the permeability of the packed diamond (or other powders) was too high to retain water for the coupling process, bubbles were removed from the column by opening the valve and allowing steady flow to flush them out, then the manometer tube was recharged with more water.

Once the diamond tube was properly coupled, the manometer was carefully filled near the top to create as much head pressure as possible. The ball valve was opened, and the system flow was allowed to establish steady state flow (a few seconds to tens of seconds depending on the permeability of the column being measured). The valve was closed, and a clean, empty, previously weighed collection beaker is quickly placed below the outlet of the diamond powder tube as shown in Figure 8 (center). The height of the head was read from the manometer (in centimeters) and

recorded as the initial height, h_o, at the initial time, $t_o = 0$. The valve was opened, and fluid allowed to drain into the collection beaker. While only one additional head measurement is required to calculate a hydraulic conductivity and subsequently a permeability, several measurements were made during the draining of the column to verify the stability of flow. The head and time measurements collected for the 125-µm and 25-µm diamond powders are summarized in Table 3.

Table 3. Falling head test measurements for 125-µm and 25-µm diamond powder packed to tap density.

125 um diamond powder

Trial #1		Trial #2		Trial #3		Trial #4	
Time (s)	Head (cm)	Time (s)	Head (cm)	Time (s)	Head (cm)	Time (s)	Head (cm)
0	79.0	0	92.0	0	92.0	0	96.5
115	63.0	41	85.0	40	85.0	32	90.0
155	58.0	84	78.0	71	80.0	86	80.0
190	54.0	138	70.0	102	75.0	146	70.0
271	46.0	213	60.0	135	70.0	214	60.0
340	40.0	298	50.0	208	60.0	292	50.0
404	35.0	399	40.0	291	50.0	382	40.0
492	29.0	518	30.0	387	40.0	491	30.0
557	25.0	559	27.0	506	30.0	554	25.0
				533	28.0	624	20.0
						671	17.0

25 um diamond powder

Trial #1		Trial #2		Trial #3		Trial #4	
Time (s)	Head (cm)	Time (s)	Head (cm)	Time (s)	Head (cm)	Time (s)	Head (cm)
0	96.5	0	96.5	0	94.9	0	97.3
320	94.5	1567	94.5	421	92.0	399	94.5
989	90.2	3186	90.2	2366	80.0	2348	82.5
1583	86.5	4710	86.5	4354	69.0	6180	62.5
2364	82.0	6927	82.0	7826	53.0	7880	55.0
4847	68.5	8913	68.5	8057	52.0	8365	53.0
6406	61.0	8986	61.0				
9148	49.5						
9271	49.0						

5. Discussion of Results

5.1 Diamond Powder Characterization

The as-received diamond grit was found to be uniform and consistent with the vendor reported sizes. The median size of 127.4 µm is slightly higher than the target 125-µm size, but the modal size is approximately equivalent at 125.6 µm. The cuboctahedral diamond has a more uniform aspect ratio, approaching sphericity, and smooth faceted surfaces, which are expected to contribute to more uniform packing and idealized behavior. The packing fraction of 64.4% is slightly higher than RCP, but entirely within expectations. It has been shown that as the particle size distribution broadens, the contribution of particles larger than the mean

influences the packing density more strongly, causing the density to increase by as much as a few percent.[21] The target packing fraction for pure monosized RCP spheres is 63.4%.[27] The 1.0% increase in packing fraction of the 100% 125-μm diamond packing would be consistent with the contribution of diamond sizes above the 125-μm mean as shown in the distribution of Figure 7. Additionally, the large mass of 125-μm diamond, and therefore gravitational force, of the particles would dominate weaker electrostatic forces that tend to agglomerate smaller powders. By comparison, however, the 25-μm particles were found to pack to a lower fraction, 60.6%, than RCP. This can be attributed to two main influences: the deviation of the size from a spherical aspect ratio owing to their crushed morphology and the smaller-sized powder being influenced by electrostatic forces that bind lighter particles together and prevent optimal packing.[21]

5.2 Packing of Diamond Powder

The bimodal mixtures of 125-μm and 25-μm diamond demonstrate a peak in packing fraction at the contribution of 80 vol% of the larger size as recorded in Table 2. Simulations of frictionless spherical particles for several size ratios are shown in Figure 9 (left), where the 5:1 size ratio has a peak packing fraction of about 78% at 79 vol% large particles (21% small). The measured packing fraction of 82% for the 80/20 diamond mixture is notably larger at nominally the same volume fraction of large spheres, but several factors differentiate the theory and experiment. Frictional effects on particles, for example, tend to suppress packing efficiency further as evidenced in Figure 9 (right), where the red vertical line at 25% small particle volume fraction has a packing factor of 75.6% when the coefficient of sliding friction is 0.1.[36] Compared to the frictionless results at the same size ratio, just a small amount of sliding friction reduces the packing fraction by approximately 2.5% and increases the small particle volume fraction contribution by 4%. It is clear from the results that increasing the value of sliding friction correspondingly shifts optimal packing towards increased concentrations of small particles and reduce the optimal packing efficiency overall.[36] In the 80/20 mixture, the 125-μm diamond would experience minimal frictional effects relative to the particle weight with most of the mixture being larger particles and trend towards the frictionless results. However, the errors are still larger than anticipated and thus likely derive from errors in the tap density measurements, which are captured manually by visual observation of the graduated cylinder, and thus contribute a larger uncertainty to the overall measurement.

The small error notwithstanding between the experimental and theoretical packing efficiency for the 80/20 mixture, the nature of the measured diamond particle packing response plotted in Figure 10 is within the bounds of previously published

packing distributions of monosized RCP sphere mixtures as shown in Figure 9, which were derived computationally.[36,37] Similarly, the trend of experimentally measured values of permeability for mixed diamond powders in this study is consistent with the theory presented.

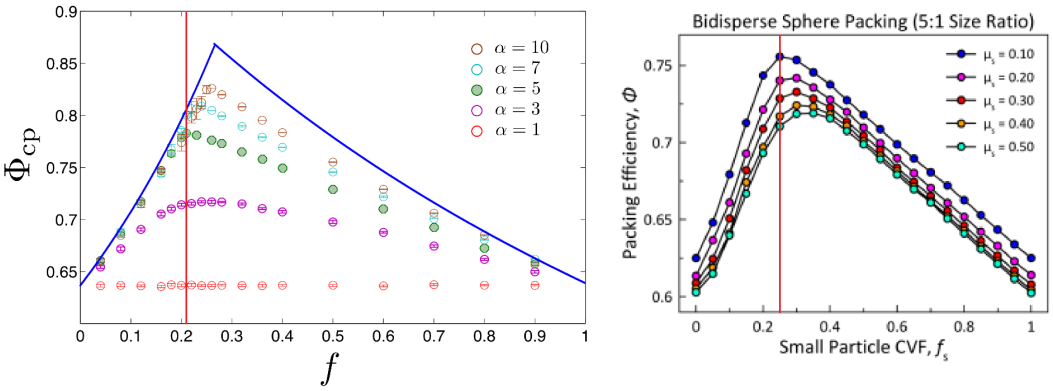

Figure 9. Computationally derived packing of ideal frictionless RCP sphere assemblies for size ratios from 1 to 10 (left). Packing fraction is plotted vertically against the volume fraction of small spheres. Size ratio of 5:1 is shown by solid green circles with a peak packing efficiency of 79% at 21% of small-diameter particles indicated by the red line. (After Prasad et al.[37]) Watkins et al.[36] introduced a sliding friction term to the packing simulations (right) that leads to reduced packing efficiency at increasing volume fraction of small particles for the same 5:1 size ratio. A 0.1 sliding coefficient of friction reduces the packing efficiency to 75.6% at a small volume fraction to 25% also shown by the red line compared to the frictionless result.[36]

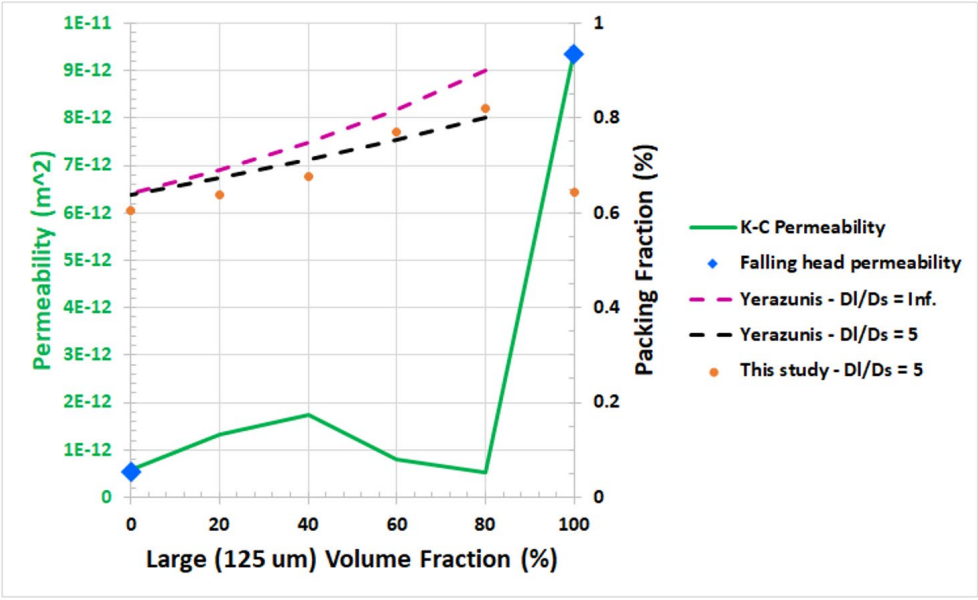

Figure 10. Permeability and packing behavior for bimodal mixtures of 125-µm and 25-µm diamond powders. Permeability is shown on the left axis and packing fraction is plotted on the right. Theoretical packing estimates from Yerazunis et al.[29] are plotted for an optimal infinite size ratio and a ratio of 5, analogous to this study. Orange circles are the measured packing behavior. The laboratory measurements of permeability (blue diamond) agree well with Kozeny–Carman empirical estimates (Equation 2).

The generalized packing relationship determined by Yerazunis et al.[29] shown in Equation 1 was used to predict the packing density of the various diamond powder mixtures in this investigation. The packing fractions are plotted in Figure 10 using the size ratio of $D_l/D_s = 5$ and volume fractions from Table 2. The value of f_{rcp} used in the calculations was 0.638 for consistency with published results, noting the previously cited value by Berryman[27] was 0.6344. The difference has negligible influence on the packing values, which are plotted in Figure 10 as the dotted black line. Reasonable agreement is found by comparing the experimentally measured packing fractions to those determined from Equation 1. The relationship of Equation 1 has reduced applicability above around 80 vol% large particles, and therefore no comparison is made with the endpoint on the graph. Also included for reference is the ideal packing limit for an infinite size ratio, shown by the dotted violet line. The packing results for the infinite ratio help establish the validity of the experimental findings in that they are expected to be less than optimal packing density, which is what was observed.

5.3 Permeability of Diamond Powder Packings

The falling head measurements of Table 3 can be used in conjunction with Equations 3 and 4 to calculate the Darcy permeability. The permeability values calculated from the experimentally measured hydraulic conductivities on the diamond packings of 125-µm and 25-µm powders are both listed in Table 4. It was noted during the initial measurements of hydraulic conductivity for each of the powder compacts that air bubbles were entrained within the sample column. These bubbles influenced the flow of liquid, and their measurements were excluded from the averaging. The average Darcy permeability determined from the measurements from trials 2–4 was found to be 9.34×10^{-12} m^2 for the 125-µm diamond packing at 64.4% dense and 5.31×10^{-13} m^2 for the 25-µm diamond packing at 60.6% dense. These values are plotted in the graph of Figure 10 as blue diamonds.

Table 4. Summary of hydraulic conductivities, *K*, and corresponding permeability, *k*, from falling head permeability tests for 125-µm and 25-µm diamond powders. Hydraulic conductivity units are m/s and permeability have units of m^2. The first trial for each size was influenced by bubbles entrained in the test chamber and thus were excluded from the average.

	125 µm		25 µm	
Trial #	*K*	*k*	*K*	*k*
1	8.38E-05	8.6E-12	4.2E-06	4.2E-13
2	9.16E-05	9.4E-12	5.9E-06	6.1E-13
3	9.7E-05	9.9E-12	4.9E-06	5.0E-13
4	8.53E-05	8.7E-12	4.7E-06	4.8E-13

As the packings used in this study were sufficiently porous, the Kozeny–Carman relationship of Equation 2 was used to estimate permeability and compare with the experimental findings. While the Kozeny–Carman relationship was derived for monosized granular materials, a reasonable estimate can be made of particle size by averaging the mixed packings. Thus, for the powder blends in Table 2, a rule of mixtures was used to establish a mean particle size, which was then used to calculate the permeability using Equation 2. The mean particle size used in the calculations is also listed in Table 2. The permeability results are plotted alongside the experimental measurements in Figure 10 where the Kozeny–Carman permeability for 125-μm diamond was 9.44×10^{-12} m^2 and the 25-μm diamond was 5.78×10^{-13} m^2. The 125-μm results agree within about 1%, and the 25-μm results agree within about 8%. Further evaluation of the bimodal mixtures of diamond powders indicated a peak permeability around 40 vol% large diamond, which occurs around 75% packing fraction for the mixture. Moreover, the trend is that for an increasing volume fraction of large particles above 40 vol%, the packing fractions of diamond increase and the permeability drops to the point where a maximum packing fraction is achieved. At that point, permeability starts to increase again until a maximum permeability is obtained for the monomodal size (100% large). The change is more rapid on the large side of the graph and not captured experimentally with the 20 vol% increments of this study. However, this trend is to be expected as the available pore space increases as demonstrated phenomenologically in Figures 1 and 9.

These packing permeability results help elucidate the complex interactions of granular diamond mixtures. In the context of synthesizing LSI composites, these results illustrate the need for careful optimization. Generally, the trend for increased performance of diamond-SiC composites is towards higher diamond fractions. Increased diamond content for LSI composites has shown benefits, especially for thermal conductivity.[38,39] Many mechanical properties of diamond-SiC composites are likewise improved with increased diamond content. Therefore, the goal of LSI composite synthesis depends on identifying diamond powder mixtures that maximize the packing fraction of diamond but without limiting the infiltration pathways and preventing optimal densification. Infiltration pathway optimization is only part of the necessary formula for improved composite synthesis, but as the initial melt infiltration depends strongly on the available pathways, it is deemed an important criterion to control.

Another complication is that the infiltrating silicon reacts with exposed diamond to convert it to non-diamond carbon and then SiC. This will reduce the final diamond packing fraction and composite density, which drives the need to increase the initial packing fraction as much as possible to compensate for the conversion loss of

diamond. Though the amount of diamond that converts to non-diamond carbon will vary based on its size, the surface (faceted versus fractured), and thermal processing conditions, the need to maximize a given diamond packing fraction remains.

One can observe the permeability results of Figure 10 relative to the increasing volume fraction of large diamond particles and increased packing fraction of bimodal diamond and note that attempts to increase packing fraction will have corresponding reductions in permeability. For this bimodal mixture, it is noted that reducing the volume fraction of large diamond towards the peak permeability at 40 vol% may represent a region of optimization for LSI formulations. Future development goals will focus on gaining insight by balancing these trends and demonstrating them in bulk composite synthesis.

6. Conclusion

This investigation characterized packing and permeability behavior for bimodal mixtures of 125 μm and 25 μm diamond powders using a falling head permeability test and comparing results to well-established theoretical and computational results for idealized spheres. The laboratory measurements of Darcy permeability were 9.44×10^{-12} m^2 and 5.78×10^{-13} m^2 for the 125 μm and 25 μm packed diamond respectively. The permeabilities were collected for diamond powders at their tap densities of 64.4% (125 μm) and 60.6% (25 μm) and agreed strongly with predictions by a well-established empirical Kozeny–Carman relationship. The overall packing behavior of bimodal mixtures of diamond was consistent within theoretical and computational values and the Kozeny–Carman permeability estimates demonstrated a peak permeability at 40 vol% large diamond, which can be used in future LSI composite development optimization where increasing diamond packing fraction reduces available permeability for the composite synthesis but is necessary to optimize material performance for most applications.

7. References

1. Rhodes MJ. Principles of powder technology. Wiley; 1990.
2. Higashitani K, Makino H, Matsusaka S, editors. Powder technology handbook. 4th ed. CRC Press; 2019.
3. Upadhyaya GS. Powder metallurgy technology. Cambridge International Science Publishing; 1997.
4. Kingery WD, Bowen HK, Uhlmann DR. Introduction to ceramics. John Wiley & Sons; 1976. Vol. 17.
5. Hillig WB. Melt infiltration approach to ceramic matrix composites. J Am Ceram Soc. 1988;71(2):C–96.
6. Michaud V, Mortensen A. Infiltration processing of fibre reinforced composites: governing phenomena. Compos Part A Appl Sci Manuf. 2001;32(8):981–996.
7. Sree Manu KM, Ajay Raag L, Rajan TPD, Gupta M, Pai BC. Liquid metal infiltration processing of metallic composites: a critical review. Metallurg Mater Trans B. 2016;47:2799–2819.
8. Arai Y, Inoue R, Goto K, Kogo Y. Carbon fiber reinforced ultra-high temperature ceramic matrix composites: a review. Ceram Int. 2019;45(12):14481–14489.
9. Herrmann M et al. Diamond-ceramics composites—new materials for a wide range of challenging applications. J Euro Ceram Soc. 2012;32(9):1915–1923.
10. Matthey B et al. SiC-bonded diamond materials produced by pressureless silicon infiltration. J Mater Res. 2017;32(17):3362–3371.
11. Margiotta JC, Zhang D, Nagle DC, Feeser CE. Formation of dense silicon carbide by liquid silicon infiltration of carbon with engineered structure. J Mater Res. 2008;23(5):1237–1248.
12. Toy C, Scott WD. Ceramic-metal composite produced by melt infiltration. J Am Ceram Soc. 1990;73(1):97–101.
13. Hofbauer PJ, Rädlein E, Raether F. Fundamental mechanisms with reactive infiltration of silicon melt into carbon capillaries. Adv Eng Mater. 2019;21(8):1900184.

14. Ershov AEE, Shikunov SL, Kurlov VN. Method of calculating the phase composition of SiC–Si–C materials obtained by silicon infiltration of carbon matrices. Tech Phys. 2017;62:903–910.

15. Sato Y et al. Viscosity of molten silicon and the factors affecting measurement. J Cryst Growth. 2003;249(3–4):404–415.

16. Sasaki H, Tokizaki E, Huang XM, Terashima K, Kimura SKS. Temperature dependence of the viscosity of molten silicon measured by the oscillating cup method. JJAP. 1995;34(7R):3432.

17. Lumay G et al. Measuring the flowing properties of powders and grains. Powder Technol. 2012;224:19–27.

18. Groarke R, Vijayaraghavan RK, Powell D, Rennie A, Brabazon D. Powder characterization—methods, standards, and state of the art. In: Yadroitsev I, Yadroitsava I, du Plessis A, MacDonald E, editors. Fundamentals of Laser Powder Bed Fusion of Metals. Elsevier; 2021. p. 491–527.

19. ASTM B527. Standard test method for determination of tap density of metallic powders and compounds. American Society for Testing Materials; 2006.

20. Abdullah EC, Geldart D. The use of bulk density measurements as flowability indicators. Powder Technol. 1999;102(2):151–165.

21. German RM. Particle packing characteristics. Metal Powder Industries Federation; 1989.

22. Cumberland DJ, Crawford RJ. The packing of particles. 1987.

23. Furnas CC. Grading aggregates-I.-Mathematical relations for beds of broken solids of maximum density. Ind Eng Chem. 1931;23(9):1052–1058.

24. Furnas CC. Flow of gases through beds of broken solids. Department of Commerce (US); 1929. Bulletin No.: 307.

25. Andreasen AHM. Ueber die beziehung zwischen kornabstufung und zwischenraum in produkten aus losen körnern (mit einigen experimenten). Kolloid-Zeitschrift. 1930;50:217–228.

26. Westman AR, Hugill HR. The packing of particles 1. J Am Ceram Soc. 1930;13(10):767–779.

27. Berryman JG. Random close packing of hard spheres and disks. Physical Rev A. 1983;27(2):1053.

28. McGeary R. Mechanical packing of spherical particles. J Am Ceram Soc. 1961;44(10):513–522.

29. Yerazunis S, Cornell SW, Wintner B. Dense random packing of binary mixtures of spheres. Nature. 1965;207(4999):835–837.

30. Neuman SP. Theoretical derivation of Darcy's law. Acta Mechanica. 1977;25(3):153–170.

31. Fredrich JT, DiGiovanni AA, Noble DR. Predicting macroscopic transport properties using microscopic image data. J Geophys Res Solid Earth. 2006;111(B3).

32. Berryman JG, Blair SC. Kozeny–Carman relations and image processing methods for estimating Darcy's constant. J Appl Phys. 1987;62(6):2221–2228.

33. ASTM D5856-15. Standard test method for measurement of hydraulic conductivity of porous materials using a rigid-wall, compaction-mold permeameter. ASTM International; 2015. https://doi.org/10.1520/D5856-15

34. Pedescoll A, Samsó R, Romero E, Puigagut J, García J. Reliability, repeatability and accuracy of the falling head method for hydraulic conductivity measurements under laboratory conditions. Ecol Eng. 2011;37(5):754–757.

35. Mayer-Laigle C, Gatumel C, Berthiaux H. Mixing dynamics for easy flowing powders in a lab scale Turbula® mixer. Chem Eng Res Des. 2015;95:248–261.

36. Watkins B, Hernandez-Rivera E, Guziewski M. A computational study on the effect of initial powder packing configuration on final sintered part microstructures. DEVCOM Army Research Laboratory (US). 2024. Report No.: ARL-TR-9434.

37. Prasad I, Santangelo C, Grason G. Subjamming transition in binary sphere mixtures. Phys Rev E. 2017;96(5):052905.

38. Matthey B, Kunze S, Kaiser A, Herrmann M. Thermal properties of SiC-bonded diamond materials produced by liquid silicon infiltration. Open Ceram. 2023;15:100386.

39. Schöne J, Beckert W, Matthey B, Herrmann M. Modelling of the microstructure and thermal conductivity of SiC-bonded diamond materials. Open Ceram. 2024;18:100594.

List of Symbols, Abbreviations, and Acronyms

3D	three-dimensional
ID	inner diameter
LSI	liquid silicon infiltration
RCP	random close packing
RMI	reactive metal infiltration
rpm	revolutions per minute
SEM	scanning electron microscopy
SiC	silicon carbide

1 (PDF)	DEFENSE TECHNICAL INFORMATION CTR DTIC OCA
1 (PDF)	DEVCOM ARL FCDD RLB CI TECH LIB